Contrib. Plasma Phys. **51**, No. 10, 906 – 919 (2011) / **DOI** 10.1002/ctpp.201100102

Enhancement of VUV Emission from a Coaxial Xenon Excimer Ultraviolet Lamp Driven by Distorted Bipolar Square Voltages

S. Y. Jou[1], **C. T. Hung**[1], **Y. M. Chiu**[1], **J. S. Wu**[1]*, and **B. Y. Wei**[2]

[1] Department of Mechanical Engineering, National Chiao Tung University, Hsinchu, Taiwan
[2] High-Efficiency Gas Discharge Lamps Group, Material and Chemical Research Laboratories, Hsinchu, Taiwan

Received 20 October 2010, revised 06 May 20011, accepted 09 May 2011
Published online 27 June 2011

Key words Xenon lamp, fluid modeling, excimer, coaxial.

Enhancement of vacuum UV emission (172 nm VUV) from a coaxial xenon excimer UV lamp (EUV) driven by distorted 50 kHz bipolar square voltages, as compared to that by sinusoidal voltages, is investigated numerically in this paper. A self-consistent radial one-dimensional fluid model, taking into consideration non-local electron energy balance, is employed to simulate the discharge physics and chemistry. The discharge is divided into two three-period portions; these include: the pre-discharge, the discharge (most intense at 172 nm VUV emission) and the post-discharge periods. The results show that the efficiency of VUV emission using the distorted bipolar square voltages is much greater than when using sinusoidal voltages; this is attributed to two major mechanisms. The first is the much larger rate of change of the voltage in bipolar square voltages, in which only the electrons can efficiently absorb the power in a very short period of time. Energetic electrons then generate a higher concentration of metastable (and also excited dimer) xenon that is distributed more uniformly across the gap, for a longer period of time during the discharge process. The second is the comparably smaller amount of "wasted" power deposition by Xe_2^+ in the post-discharge period, as driven by distorted bipolar square voltages, because of the nearly vanishing gap voltage caused by the shielding effect resulting from accumulated charges on both dielectric surfaces.

1 Introduction

Because of its relatively low cost and low pollution, the excimer ultraviolet (EUV) lamp has found wide applications since its debut in a form of dielectric barrier in xenon gas in 1988 [1]. These include, for example, surface cleaning [2], plasma display [3], LCD backlighting [4], water quality purification [5], material deposition [6] and material processing [7] in the semiconductor industry. EUV lamp emission is caused by the excimer falling from excited states to the ground state. An excimer (originally short for excited dimer) is an unstable dimeric with a lifetime of about 10 ns. The important features of an excimer include: emission with narrow wavelength bandwidth, high efficiency and without constraint of radiation of direction. Two typical examples are the formation of Xe_2^* or $XeC1^*$ excimer complexes. The EUV lamp has a dielectric barrier-type discharge which is a high-pressure non-equilibrium transient discharge. A primary function of the dielectric barrier is that it can suppress the occurrence of arc discharge, thereby preventing damage to the metallic electrodes. Because the plasma physics and chemistry inside the EUV lamp are complex and thus difficult to measure, its design still heavily depends on the trial-and-error method that is both time-consuming and costly. Thus, detailed simulation of excimer discharge physics and chemistry could become a viable method for understanding the complicated plasma physics inside the lamp which, in turn, would lead to a better design.

Traditional xenon DBD lamps are driven by sinusoidal voltage waveforms, with discharge efficiency typically in the range of 10-20 %, and the discharge consisting of multiple narrow filamentary channels [8]. A dramatic increase in efficiencies of up to 40 % has been demonstrated experimentally (included transmission losses through the quartz and geometric loss) by using short pulsed voltages ($<$750 ns) interrupted by long idle periods ($\sim 40\ \mu$s) [9]. Simulation of xenon DBD driven by sinusoidal voltage waveforms using the one-dimensional planar fluid

* Corresponding author. E-mail: chongsin@faculty.nctu.edu.tw, Phone: +886 3 573 1693, Fax: +886 3 611 0023

modeling has been proposed with gas pressures and frequencies in the range of 10-400 torr and 50 kHz – 1 MHz, respectively, by Oda et al. [10]. Zvereva and Gerasimov [11] computed the species population in a xenon barrier discharge under various E/Ns. Carman and Mildren [12] found that VUV generation efficiency could reach 61 % using very short voltage pulses through one-dimensional planar fluid modeling. Beleznai et al. [13] compared the simulations results of a xenon EUV lamp (75 torr, driven by short voltage pulses) with the experimental data to validate their model using one-dimensional planar fluid modeling with complex plasma chemistry in up to 99 reaction channels. Avtaeva and Kulumbaev [14] have analyzed the difference of simulations between two different chemical reaction processes. Jou et al. [15] conducted extensive parametric study of the VUV emission (172 nm) from a co-axial excimer xenon lamp driven by realistic pulsed voltages. Results show that larger rate of voltage rising will improve the absorption of electric power by electrons, which leads to a higher VUV emission efficiency. However, detailed studies about a coaxial EUV lamp driven by pulsed voltages that has explored VUV emission enhancement as compared to that driven by sinusoidal voltages is still lack in the literature, although this type of lamp may be one of the most popular types in practice.

Thus, the aim of the present study is to provide detailed simulation results of the discharge physics and chemistry in a popular coaxial-type xenon EUV lamp driven by distorted bipolar square voltages through self-consistent radial one-dimensional fluid modeling. Enhancement of VUV emission, based on the simulation results as compared to the sinusoidal case, is emphasized in this paper.

The remainder of the paper has been organized as follows. Fluid modeling is introduced next, comprising modeling equations, numerical method, use of plasma chemistry and simulation conditions. The results are then presented and discussed where applicable. Finally, major findings of the present study are summarized.

2 Numerical Method

2.1 Fluid Modeling

The fluid modeling for a homogenous radial one-dimensional discharge includes a self-consistent solution of the continuity equations (electron, ions and neutrals), the electron energy density equation and the electrostatic Poisson equations. Finite difference method is used to discretize these equations. Discretized equations are solved implicitly. Corresponding numerical schemes and estimation of transport coefficients and rate constants of reaction channels are described in detail in [15, 16] and are not repeated here for brevity.

2.2 Discharge Current, Dielectric Voltage and Gap Voltage

The discharge current $i_{\mathrm{T}}(t)$ is the sum of the conduction current $i_{\mathrm{C}}(t)$ and the displacement current $i_{\mathrm{D}}(t)$:

$$i_{\mathrm{T}}(t) = i_{\mathrm{C}}(t) + i_{\mathrm{D}}(t) \tag{1}$$

The voltage between the electrodes $\mathrm{V_s}(t)$ is given as:

$$\mathrm{V_s}(t) = \mathrm{V_d}(t) + \mathrm{V_g}(t) \tag{2}$$

where $\mathrm{V_d}(t)$ is the dielectric voltage and $\mathrm{V_g}(t)$ is the gap voltage.

2.3 Accumulated charge

Evolution of surface charge density (σ) on the dielectric barrier is calculated by integrating the fluxes of charged particles directed to the barrier surface as

$$\frac{\partial \sigma}{\partial t} = \sum e \left(\vec{\Gamma}_i - \vec{\Gamma}_e \right) \cdot \vec{n} \tag{3}$$

where $\vec{\Gamma}_i$ and $\vec{\Gamma}_e$ are the incident ion and electron flux vectors, respectively, at the barrier surface, and $\vec{n}$ is the unit normal vector of barrier surface. Note it is assumed that charges remain on the barrier surface until recombining with charges of opposite sign.

2.4 VUV Emission Efficiency

Since we only considered one-dimensional radial fluid modeling, the input power density, $P_{\rm in}$ (or dissipated power), to the discharge is thus defined as:

$$P_{in} = \frac{2}{T(r_2^2 - r_1^2)} \int_0^T \int_{r_1}^{r_2} j_c(r,t) r dr dt \tag{4}$$

where T is the period of the applied voltage and j_c is the conduction current density caused by the electrons and ions. Note that r_1 and r_2 are the inner and outer radii of the gas gap, and are fixed as 0.8 and 1.25 cm, respectively, in the current study. The VUV (vacuum UV) light output power density, $P_{out,k}$, generated from the kth kind of excited species, is defined as:

$$P_{out,k} = \frac{h\nu_k}{T(r_2^2 - r_1^2)} \int_0^T \int_{r_1}^{r_2} \frac{n_k(r,t)}{\tau_k} r dr dt \tag{5}$$

where $h\nu_k$, τ_kk and n_k are the photon energy of the VUV light, lifetime and concentration of the excimer species, respectively. Thus, the VUV emission efficiency due to k^{th} excimer species is given as:

$$\eta_k = \frac{P_{out,k}}{P_{in}} \,. \tag{6}$$

2.5 Xenon Plasma Chemistry

In the current study, we have selected the xenon plasma chemistry that is basically the same as that used in Oda et al. [10], which consists of 9 species and 24 reaction channels, as listed in Table 1. These reaction channels included electron-neutral elastic collision (No. 1 in Table 1), direct electron impact ionization (No. 2 in Table 1), excitation (No. 3-5 in Table 1), stepwise ionization (No. 6 in Table 1), recombination (No. 7 in Table 1), heavy particle collision (No. 8-18 in Table 1) and radiation process among electrons, ions, associated excited atoms, excimer xenon and ground-state xenon atoms (No. 19-24 in Table 1). Fig. 1 shows schematically these reaction channels using the energy diagram for a better overview of the inter-relation among the species.

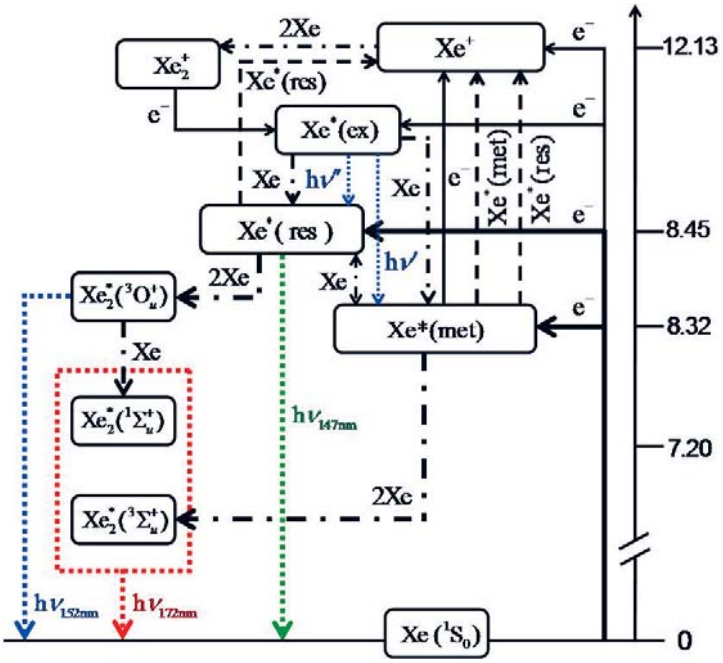

Fig. 1 Reaction processes in a Xe discharge.

Table 1 Reaction channels of the xenon discharge

No	Reaction	ε_e (eV)	Reaction rate
Momentum transfer			
1	$e^- + Xe \rightarrow Xe + e^-$	0.0	Bolsig [15]
Imoact ionization			
2	$e^- + Xe \rightarrow Xe^+ + 2e^-$	12.1	Bolsig [15]
Excitation			
3	$e^- + Xe \rightarrow Xe^*(ex) + e^-$	9.57	Bolsig [15]
4	$e^- + Xe \rightarrow Xe^*(res) + e^-$	8.44	Bolsig [15]
5	$e^- + Xe \rightarrow Xe^*(met) + e^-$	8.32	Bolsig [15]
	Stepwise ionization		
6	$e^- + Xe^*(met) \rightarrow Xe^+ + 2e^-$	3.44	Bolsig [15]
	Recombination		
7	$e^- + Xe_2^+ \rightarrow Xe^*(ex) + Xe$	11.1	$2.0\times10^{-7}\,T_e^{-0.5}\mathrm{cm^3s^{-1}}$ [10]
Conversion to excited state			
8	$Xe^*(ex) + Xe \rightarrow Xe^*(res) + Xe$	0.0	$2.0\times10^{-11}\,\mathrm{cm^3s^{-1}}$ [10]
9	$Xe^*(ex) + Xe \rightarrow Xe^*(met) + Xe$	0.0	$2.0\times10^{-11}\,\mathrm{cm^3s^{-1}}$ [10]
10	$Xe^*(res) + Xe \rightarrow Xe^*(met) + Xe$	0.0	$2.2\times10^{-14}\,\mathrm{cm^3s^{-1}}$ [10]
11	$Xe^*(met) + Xe \rightarrow Xe^*(res) + Xe$	0.0	$1.5\times10^{-15}\,\mathrm{cm^3s^{-1}}$ [10]
Conversion to dimers			
12	$Xe^*(res) + 2Xe \rightarrow Xe_2^*(o_u^+) + Xe$	0.0	$1.55\times10^{-31}\,\mathrm{cm^6s^{-1}}$ [10]
13	$Xe^*(met) + 2Xe \rightarrow Xe_2^*(^3\sum_u^+) + Xe$	0.0	$8.53\times10^{-32}\,\mathrm{cm^6s^{-1}}$ [10]
14	$Xe_2^*(O_u^+) + Xe \rightarrow Xe_2^*(^1\sum_u^+) + Xe$	0.0	$8.7\times10^{-11}\,\mathrm{cm^3s^{-1}}$ [10]
Excited -excited collision induced ionization			
15	$Xe^*(res) + Xe^*(res) \rightarrow Xe^+ + Xe + e^-$	0.0	$5.0\times10^{-10}\,\mathrm{cm^3s^{-1}}$ [10]
16	$Xe^*(met) + Xe^*(met) \rightarrow Xe^+ + Xe + e^-$	0.0	$5.0\times10^{-10}\,\mathrm{cm^3s^{-1}}$ [10]
17	$Xe^*(res) + Xe^*(met) \rightarrow Xe^+ + Xe + e^-$	0.0	$5.0\times10^{-10}\,\mathrm{cm^3s^{-1}}$ [10]
Ion conversion (three-body collision)			
18	$Xe^+ + Xe + Xe \rightarrow Xe_2^+ + Xe$	0.0	$8.0\times10^{-32}\,\mathrm{cm^6s^{-1}}$ [10]
VUV emission			
19	$Xe_2^*(^1\sum_u^+) \rightarrow 2Xe + h\nu(172\,nm)$	0.0	$1.82\times10^{8}\,\mathrm{s^{-1}}$ [10]
20	$Xe_2^*(^3\sum_u^+) \rightarrow 2Xe + h\nu(172\,nm)$	0.0	$1.0\times10^{7}\,\mathrm{s^{-1}}$ [10]
21	$Xe_2^*(O_u^+) \rightarrow 2Xe + h\nu(152\,nm)$	0.0	$9.0\times10^{6}\,\mathrm{s^{-1}}$ [10]
22	$Xe^*(res) \rightarrow Xe + h\nu(147\,nm)$	0.0	$4.3\times10^{5}\,\mathrm{s^{-1}}$ [10]
Radiation to lowerlevel (visible and infrared)			
23	$Xe^*(ex) \rightarrow Xe^*(res) + h\nu'$	0.0	$2.7\times10^{7}\,\mathrm{s^{-1}}$ [10]
24	$Xe^*(ex) \rightarrow Xe^*(res) + h\nu''$	0.0	$2.53\times10^{7}\,\mathrm{s^{-1}}$ [10]

2.6 Simulation Conditions

Fig. 2 depicts a sketch of the coaxial xenon excimer lamp simulated in the present study. The tube length is 70 cm, the gap distance in the radial direction is 4.5 mm, and both the inner and outer quartz tubes are 1 mm thick. An inner-powered electrode with a radius of 7 mm, is placed in direct contact with the inner quartz tube and an outer mesh grounded electrode ($\sim$ 92 % in porosity) with a radius of 13.5 mm, is placed outside the outer quartz tube. The complicated three-dimensional geometrical structure is simplified as a one-dimensional radial coordinate system in the current study, as the first step in understanding the discharge physics and chemistry without the complications of geometry. The dielectric constant of the quartz tube is 4.0, and pulsed power supply frequency f and xenon gas pressure p are fixed at 50 KHz and 380 torr, respectively, throughout the study. Note

that we have only presented the detailed discharge properties for the case of distorted square voltages, since the results of the case of sinusoidal voltages are essentially similar.

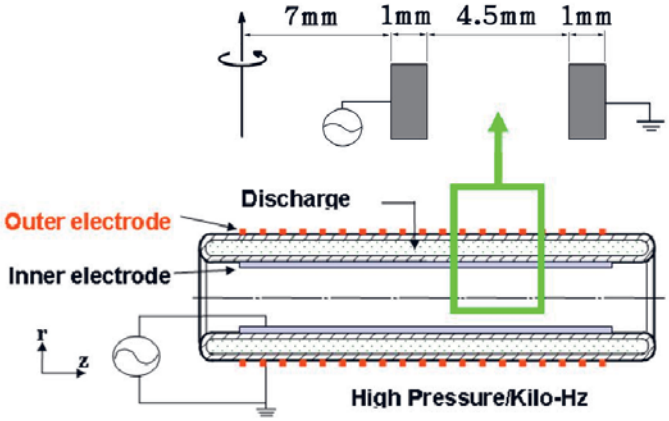

Fig. 2 The configuration of a DBD lamp.

In the simulations, time step size varies automatically based on the constrained CFL condition and dielectric relaxation time step. Since we employed fully implicit algorithm for solving the coupled discretized equations, our experience shows that the resulting time step size is generally 5-10 times larger than the above two mentioned constrained conditions. Initial conditions are generally set up as a uniform quasi-neutral distribution of charged particles with the order of $10^{11}\mathrm{cm}^{-3}$. Generally 3-5 cycles are found to be enough for reach quasi-steady state as presented in the current study.

3 Results and Discussion

3.1 Qualitative Validation of the Model

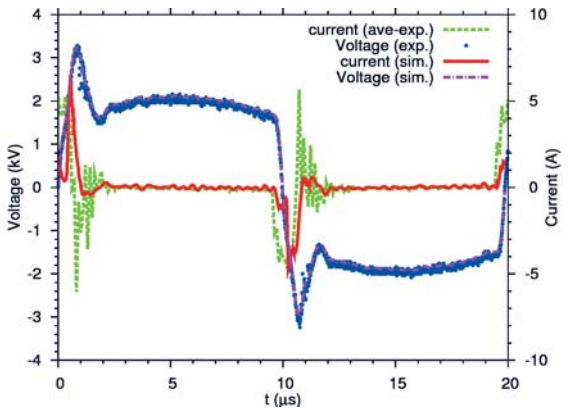

Fig. 3 The comparison with simulated result and experimental data.

Fig. 3 shows the qualitative comparison of the simulated and the experimental discharge currents in a cycle. Note that the experiments will be described in detail in another study in the near future. Several fast oscillating current spikes are found from the measured currents, while only a single major spike is found from the simulated data. The former shows that it is a typical type of microdischarge. Interestingly, the magnitude of the simulated spike is qualitatively comparable to that of the measured data. Note that the actual EUV lamp had a very complex three-dimensional geometric structure with a highly porous outer grounded electrode. Also, the measured voltages are slightly more positive at the inner electrode than at the outer electrode in the post-discharge period, which is attributed to the auto-DC-bias effect because of the unequal area of the inner and outer electrodes (~ 5 to 1). Note that the slightly negative current is within the experimental uncertainties of the current probe. In the current study, we did not take this into account in the simulation. In brief summary, we should take the above

comparison qualitatively since it is obviously the 1D fluid modeling cannot model correctly the complex 3D microdischarge behavior as expected. However, we believe that the use of the one-dimensional radial fluid model should capture qualitatively the major discharge physics inside the real EUV lamp in a global sense.

3.2 Discharge Physics and Chemistry

In this section, we have only described the discharge physics and chemistry of the xenon lamp driven by realistic bipolar square voltages in detail, while describing the corresponding phenomena by sinusoidal voltages based on the necessity and the comparison purpose. We will first describe the overview of the discharge using the phase diagrams of several key discharge properties, then the details of the discharge in each period and, finally, the temporal variation of several important spatial-averaged discharge properties.

Phase diagrams of key discharge properties

Fig. 4 shows the phase diagrams of the concentrations of the charged species electron, $Xe_2^*(^3\sum_u^+)$ and electron temperature. Note that we have only shown the results of $Xe_2^*(^3\sum_u^+)$, instead of $Xe_2^*(^1\sum_u^+)$, because the concentration of the former is much greater than the latter. We divide these phase diagrams into six periods in the temporal direction according to the temporal variation of electron number density, as only electrons can respond immediately to variations in the electric field. Periods I and IV are pre-discharge regions, Periods II and V are discharge regions and Periods III and VI are post-discharge regions. Periods II and V are further divided into two sub-periods (II-1 and II-2; V-1 and V-2). The trends of discharge in the first half cycles (I, II and III) are very similar to those of the second half cycles (IV, V and VI), except that the discharge currents are opposite to each other and there are some slight differences in the properties because of the different areas of the inner and outer electrodes. For brevity, we have only described the discharge physics and chemistry in the first half cycles (I, II and III) in detail, as those in the second half cycles are fundamentally the same, with the exception as mentioned earlier.

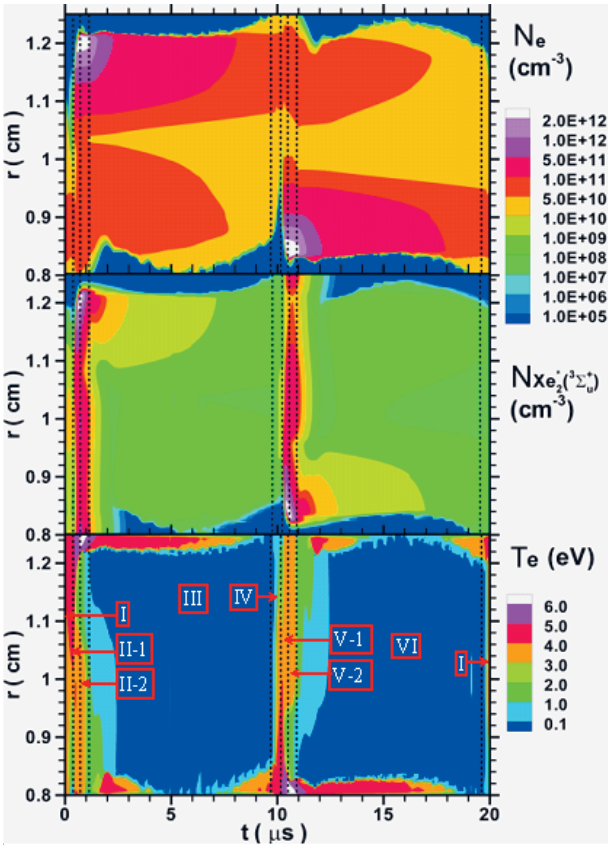

Fig. 4 Spatiotemporal diagram of number densities of excited species: electron (upper), $Xe_2^*(^3\sum_u^+)$ (middle) and electron temperature (bottom).

Period I

In this pre-discharge period, the spatial-averaged number of electrons decreased slightly with time because the electrons are attracted to the anode side (inner electrode) and accumulated on the inner dielectric tube due to its rising voltage. In the earlier part of Period I (negative applied voltage, 19.6 – 20 μs in both Fig. 4), the concentrations of all species are low, especially the excited and meatastable xenon, because the electron energy is still low in this period.

In the later part of Period I, although the electron temperatures are very high near the outer dielectric tube (cathode side) (see bottom of Fig. 4) due to the rising voltage at the inner electrode, breakdown does not occur because of the very small number of electrons existing in that region (see top of Fig. 4). At the same time, the concentrations of $Xe_2^*(^3\sum_u^+)$ increase to the order of $\sim 10^{10}$ (cm^{-3}) in the central region of the gap.

Period II

This discharge period is further divided into two sub-periods, II-1 and II-2. In Period II-1, the breakdown occurs at r$\approx$ 1 cm, where the number of electrons increased dramatically and electrons move towards the outer quartz tube at a speed of $\sim$ 7,000 m/s (from anode towards cathode) by direct electron impact ionization. We term this the "cathode-directed streamer-like" ionization wave, in which the details will be elucidated later. The number of electrons rapidly increases to the maximal value (>2 x 10^{12}cm^{-3}) within $\sim$ 0.3 μs at r $\approx$ 1.22 cm, and then decreases gradually afterwards. The amount of $Xe_2^*(^3\sum_u^+)$ is abundant across the gap because of the excitation of ground-state xenon by the still energetic electrons: Te $>$ 3 eV (Nos. 4 and 5 in Table 1).

In Period II-2, which lasts less than 4 μs, the quasi-neutral region forms across the gap with a very high plasma density ($>$ 5 x 10^{11}cm^{-3}) between the r $\approx$1.1-1.2 cm, and electrons move slowly from the cathode side (outer grounded) to the anode side (inner powered); $Xe_2^*(^3\sum_u^+)$ begins to disappear because of the intense photonemission: 172 nm (No. 20 in Table 1) in Period II-2. In the region of r $\approx$ 1.05-1.2 cm, having started in the later period of Period II-1, the electron temperature decrease rapidly with time because of the energy loss by ionization and excitation of the ground-state xenon. This will be made clear later using the snapshots of the discharge properties.

Period III

The discharge extinguished through a vanishing electric field across the gap (nearly zero) by the shielding effect, although the applied voltage is still as high as 2 kV, as will be seen clearly later through the snapshots of discharge properties. In the latter part of Period III, the electrons begins to move away from the anode side (inner) towards the cathode side (outer) at t=5-6 μs, when the applied voltage decreases from the peak (top of Fig. 6). $Xe_2^*(^3\sum_u^+)$ decreases to a very small amount ($<$10^{8}cm^{-3}), except in the early part near the cathode (outer), because the electron temperatures are very low, down to even 0.1 eV, in most of the region in Period III.

Snapshots of key discharge properties

To gain more insight into the discharge physics and chemistry, two sequential snapshots of the several key discharge properties in each period (I, II and II) are presented in Fig. 5 and described in detail in the following.

Period I

Figs. 5a and 5b show two typical snapshots of important discharge properties in the earlier and later stages of Period I, respectively. They show that the peak plasma density ($\sim$ 8 x 10^{10}cm^{-3}) is close to the anode (inner) at r $\approx$ 0.84 cm, and that it stayed nearly stationary in space, but with a very low density as compared to that of Period II, as will be shown later. However, the figures also clearly demonstrate that the electrons are attracted to the anode (inner), with the gap voltage increasing from 0.4 (Fig. 5a) to 2 kV (Fig. 5b). In the region around r $\approx$ 1 cm, the rapid growth of atomic ions, excited species (Xe^*(met)) and excimer species ($Xe_2^*(O_u^+)$, $Xe_2^*(^1\sum_u^+)$ and $Xe_2^*(^3\sum_u^+)$) could be seen due to a series of collisions by energetic electrons ($\sim$ 4 eV) moving towards the anode side (inner). On the other hand, the amount of Xe^*(res) decreased through the reactions of conversion to metastable (No. 10 in Table 1) and conversion to dimers (No. 12 in Table 1). The main collision processes of generating excited and metastable species occurred through the excitation collision channels, such as Nos. 3 and 5 in Table 1. These in turn promoted the growth of excimers through the reaction channels, such as No. 13 in Table 1, with zero threshold energy. Interestingly, the atomic ions and electrons moved towards the cathode side

(outer), which will be more clearly shown in the details of Period II. A peak value of $\sim$ 2 x $10^9 cm^{-3}$ of atomic ions (Fig. 5b) occurred at r $\approx$ 1.08 cm through the contribution of collision channels, such as Nos. 1, 6 and 16 in Table 1. Of these, the most productive channel is the electron impact ionization (No. 1 in Table 1) due to the rapid increase in voltage. As the density of the metastable species grew to a certain level, the other two channels began to contribute more in generating atomic ions.

Fig. 5 Two snapshots of total species of (a) and (b) in the period I, (c) and (d) in the period II-1, (e) and (f) in the period II-2, (g) and (h) in the period III.

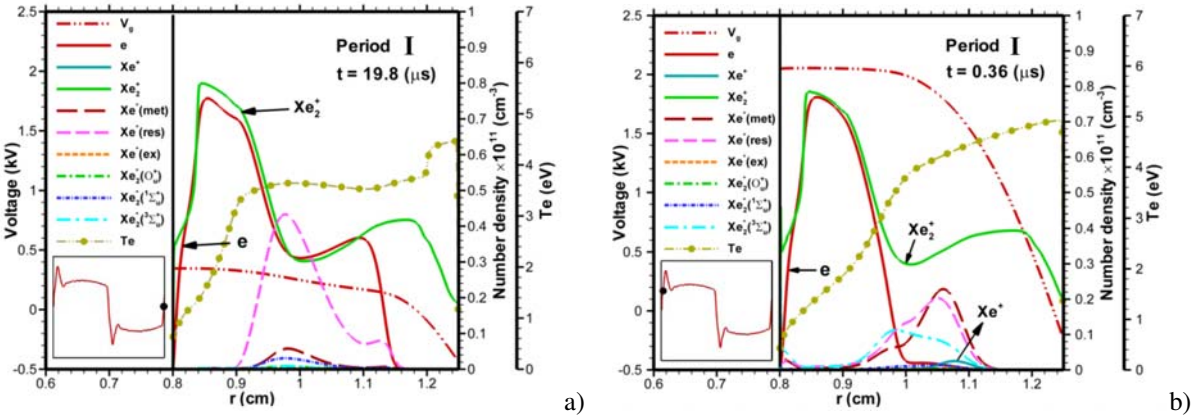

Period II

Figs. 5c and 5d present two typical snapshots of important discharge properties at earlier and later times in Period II-1, respectively. They show that the potential field is highly distorted near the cathode (outer) due to the shielding of the narrow quasi-neutral region (between r $\approx$ 1.1-1.2 cm) close to the cathode side; this in turn accelerated the few electrons near the cathode side (outer) and reached a very high electron temperature ($\sim$ 5-6 eV) (Figs. 5c and 5d) at the edge of sudden change of the electric field (r$\approx$ 1.16 cm in Fig. 5c and r $\approx$ 1.18 cm in Fig. 5d). These energetic electrons thus ionized and excited the ground-state xenon according to the reaction channels, such as Nos. 2-5 in Table 1, which could be seen clearly from the peaks of charged and excited species around r = 1.16 cm and r = 1.18 cm in Figs. 5c and 5d, respectively. At the same time, the molecular xenon ions increasingly formed through the three-body ion conversion reaction channel (No. 18 in Table 1) which reduced the atomic ions behind the right-moving head, but still maintained strict quasi-neutrality. In general, the densities of Xe^*(met) and Xe^*(res) correlated very well with the density of electrons in Period II-1, which meant that they are generated through direct electron impact reactions. An interesting phenomenon, the so-called "cathode-directed streamer-like" ionization wave, moving to the cathode is observed, in which the peak of atomic ions is ahead of that of the electrons with a speed of $\sim$ 7,000 m/s, which is far less than that of a real streamer [17].

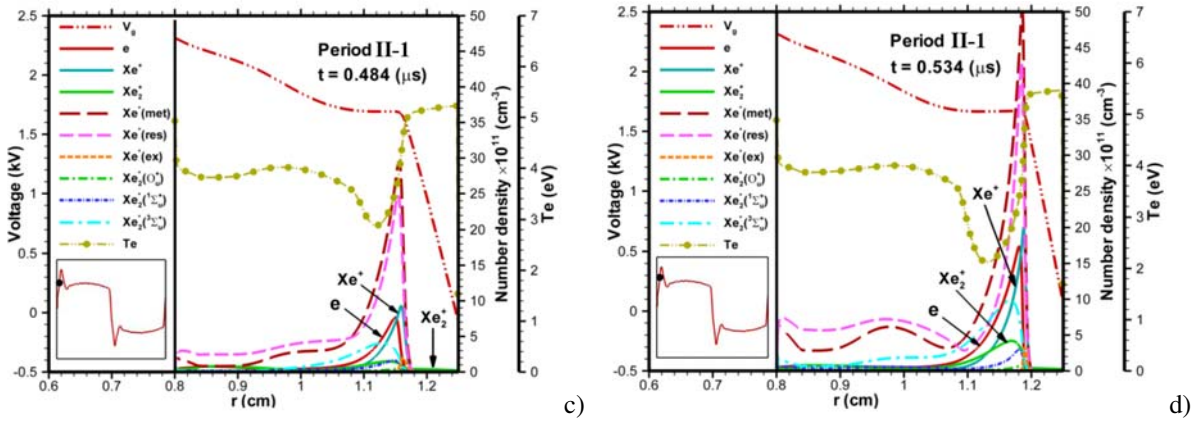

Figs. 5e and 5f present two typical snapshots of important discharge properties at earlier and later times, respectively, of Period II-2. In this period, the applied voltage almost reached its peak and the gap decreased slightly, but the stream-like ionization wave moved to a location very close to the cathode dielectric surface (outer) and stayed almost stationary in Period II-2. The peak value of electrons greatly increased to a level of $\sim$ 2.7 x 10^{12}cm^{-3} at the position of r=1.22 cm, while the dominating ion species became Xe_2^+ instead of Xe^+ through the increasingly important three-body ion conversion channel (No. 18 in Table 1). Accordingly, this rapidly consumed Xe^+. In addition, the amount of Xe^*(met) and Xe^*(ex) are greatly reduced from values of 4 x 10^{12}cm^{-3} and 2.7 x 10^{12}cm^{-3}, respectively, down to 1.5 x 10^{12}cm^{-3} and 5 x 10^{11}cm^{-3}, respectively, due to the less energetic electrons; this is caused by the reduced electric field due to the shielding by the accumulated ions at the cathode dielectrics (outer); this led to the slight reduction of $Xe_2^*(^3\sum_u^+)$ from 2.5 x 10^{12}cm^{-3} to 2 x 10^{12} cm^{-3}, which is the most important species for VUV (172 nm) emission, across the gap. After Period II-2, the discharge became more diminished, as described next.

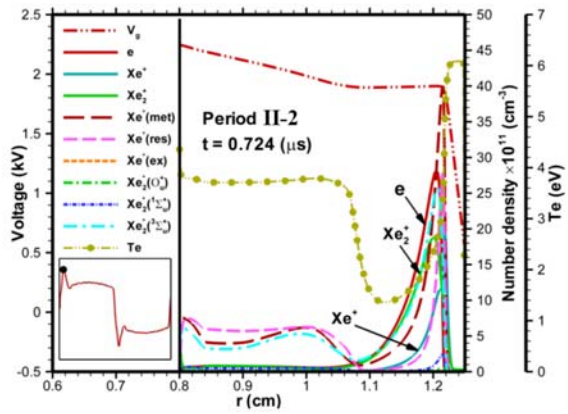

e)

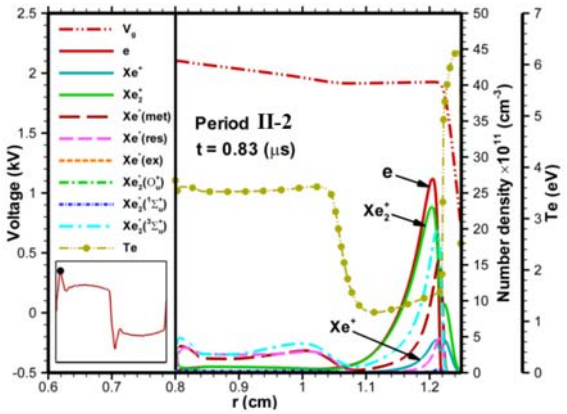

f)

Period III

Figs. 5g and 5h present two typical snapshots of important discharge properties at earlier and later times of Period III, respectively. In this period, the quasi-neutral region expanded slowly from the cathode side (outer) towards the anode side (inner) with greatly decreasing plasma density in the peak (from 8 x 10^{11}cm^{-3} to 1.1 x 10^{11}cm^{-3}) close to the cathode (outer); this is attributed to the decreasing electron temperature caused by the reduced electric field in the sheath on both sides. Especially, the electron temperature in Fig.5h is reduced to nearly zero because of the very small electric field in the sheaths. The major species in Period III are electrons and Xe_2^+, while the other species almost disappeared ($<10^9$cm^{-3}) and came into a post-discharge period (extinguished). After Period III, the polarity of the applied voltage changed and the above described pre-discharge (Period I), discharge (Period II) and post-discharge (Period III) repeated temporally with opposite direction and location because of the higher plasma density and more abundant excited species due to the stronger electric field near the inner electrode caused by the small radius of curvature.

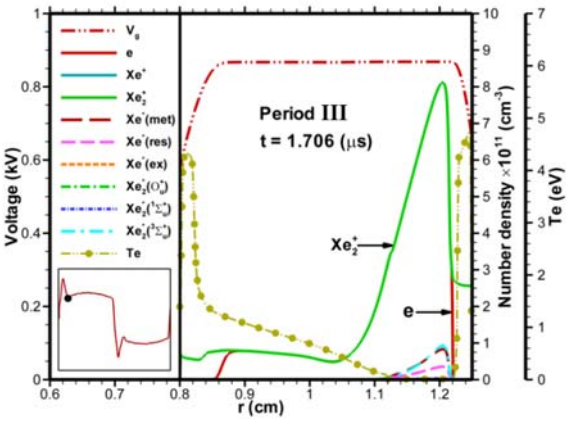

g)

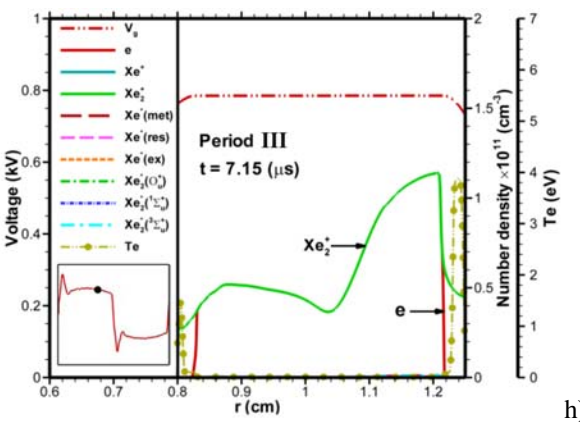

h)

Temporal variation of discharge properties

To further elucidate the discharge physics described above, we have presented the temporal variation of other discharge properties together in Fig. 6, which include: a) the applied voltage (V_a), the dielectric voltage (V_d) and the gap voltage (V_g); and b) the discharge current density at the inner side (r = 0.8 cm) and the accumulated charges (Q_a) at both dielectric surfaces (r = 0.8 and 1.25 cm). Note that the dielectric voltage is defined as the sum of voltages across both quartz tubes. Several important characteristics are drawn from Fig. 6, as follows. "Memory effects" are clearly seen throughout the cycle. For example, in Period I, the gap voltage led the applied voltage (see Fig. 6a) because of the shielding caused by the positive accumulated charges at the anode dielectric surface (inner) remnant from the previous cycle (see Fig. 6b). During the discharge period (Period II), the electrons rapidly accumulated on the inner anode dielectric surface (see Fig. 6b), which resulted in a much smaller gap voltage (see Fig. 6a) by shielding out the applied voltage. Throughout Period III, the gap voltage is almost zero (see Fig. 6a) as the surface charge density remained roughly the same on both dielectric surfaces (see Fig. 6b), although the applied voltage is almost as high as 2 kV. In addition, the magnitude of the accumulated surface charge density and current density at the inner dielectric surface is always greater than that at the outer dielectric surface because of the smaller inner area.

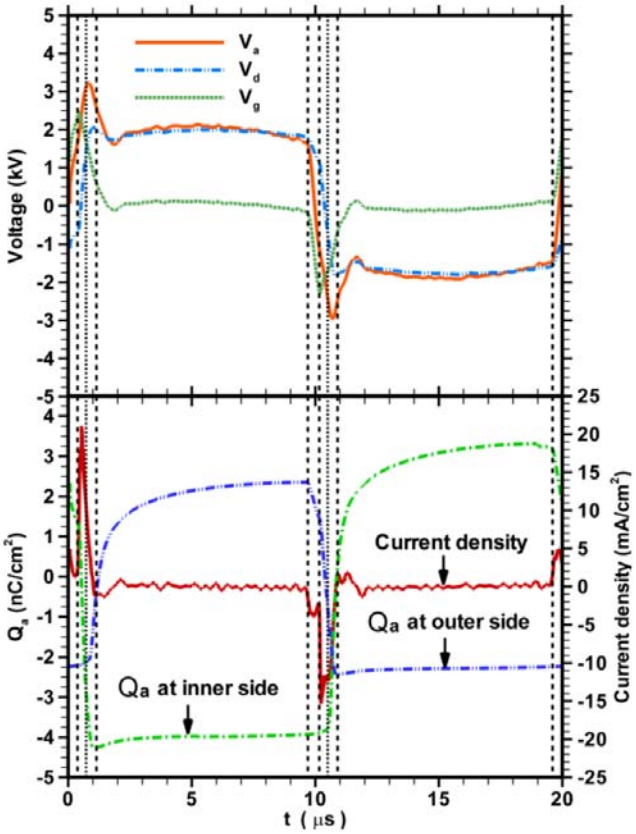

Fig. 6 The temporal variations of (a) applied voltage (V_a), dielectric voltage (V_d) and gap voltage (V_g) in upper figure (b) discharge current density at inner side (r= 0.8 cm) and accumulated charge (Q_a) in bottom figure utilizing distorted square voltages over a cycle.

Fig. 7 provides a general view of the discharge across the gap and the exposure view of several important spatial-averaged discharge properties in the first 2 μs, in which the discharge occurred. During the discharge process (Period II), from 0.4 to 1.14 μs, the molecular xenon ions initially outnumbered the atomic xenon ions. The trend did not change until 0.46 μs and lasted through 0.6 μs, in which the discharge occurred. It is also clear that the molecular xenon ions are the dominant ion species at all times, except in the very initial period of the breakdown process, as mentioned above (0.46-0.6 μs). As for the trend of spatial-averaged electron temperature, it is raised to a value of $\sim$ 4.1 eV prior to when the discharge occurred, and decreased to less than 1 eV right after the discharge process because of the loss of most of the energy via ionizations and excitations. In addition, the

peaks of Xe^*(met) (8.6 x 10^{11}cm^{-3}) and $Xe_2^*(^3\sum_u^+)$ (5.6 x 10^{11}cm^{-3}) both occurred in the early part of the discharge period (Period II-1), although the latter lagged behind the former by ~ 1 μs.

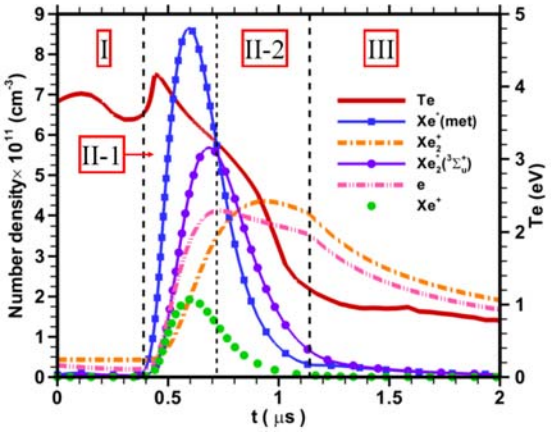

Fig. 7 The temporal variations of spatially averaged number density of electron, the ion species Xe^+ and $2Xe_2^+$, the main excited species Xe^* (met), the main excimer species $Xe_2^*(^3\sum_u^+)$ and Te during the period t = 0 $\sim$ 2 (μs).

Characteristics of Power Deposition and VUV Emission

Fig. 8 presents the volumetric power densities of various VUV emission lines and absorption by charged species over a cycle. Fig. 8a shows that the 172 nm line of VUV is the major source of VUV emission, as compared to the other two lines (147 and 152 nm). The VUV light emission originated from the process whereby both the excimer species $Xe_2^*(^1\sum_u^+)$ (less dominating) and $Xe_2^*(^3\sum_u^+)$ (most dominating) from an excited state fall to ground state. In addition, the major periods of 172 nm VUV emission occurred in Period II-1 in the first half cycle and in Period V-1 in the second half cycle, which corresponded to when Xe^*(met) and $Xe_2^*(^3\sum_u^+)$ are most abundant, as shown in Fig. 7. It is noted that the emitted power of 172 nm is greater in Period II-1 than in Period V-1 because of the "integration effect" of larger circumferential volume near the outer dielectric surface where the intense VUV emission occurred with a smaller value in Period II-1.

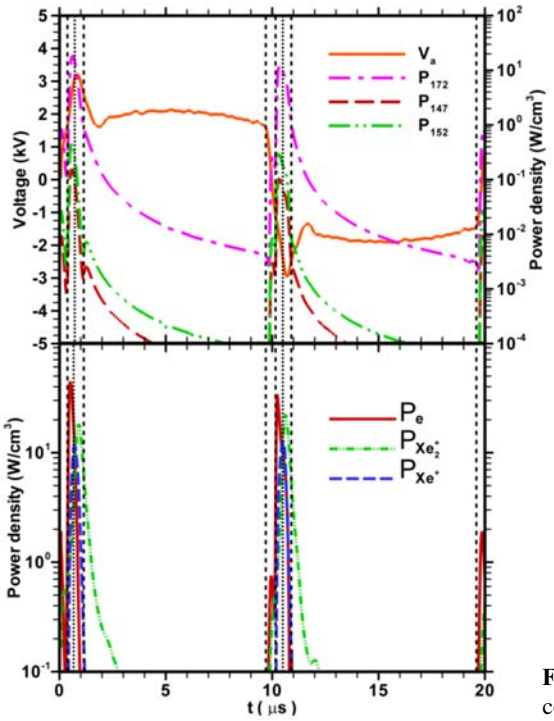

Fig. 8 The spatially integrated power emission (upper figure) and corresponding power deposition (lower figure) utilizing distorted square voltages over a cycle.

Fig. 8b shows that the volumetric absorbed power is first deposited through the electrons for a very high power density (peak value of 45 Wcm^{-3}) in a very short period of time ($\sim$ 0.35 μs) during discharge Period II-1, then partly through Xe^+ for a low power density (peak value of 12 Wcm^{-3}) in a very short period of time ($\sim$ 0.35 μs), and finally through Xe_2^+ for a medium power density (peak value of 18 Wcm^{-3}) for a longer period of time ($\sim$ 0.4 μs). Again the electrons absorbed more volumetric power in the first half cycle (Period II) than in the second half cycle (Period V), for a similar reason as mentioned above.

Comparison of VUV Emission Efficiency between Sinusoidal and Distorted Sinusoidal Voltages

Fig. 9 shows: a) P_{172} and corresponding efficiency of 172 nm VUV as defined earlier in Eq. (6); and b) the power deposition and corresponding fraction in different charged species for the two types of power source (sinusoidal and distorted bipolar square) under the same test conditions (p=380 torr; f=50 kHz; d=4.5 mm). Note that P_{172} is defined as the total VUV emission power as referred in Eq. (5). Fig. 10a shows that the emitted power density for 172 nm using distorted bipolar square voltages increased 2.5 times (from 49.2 to 124.8 mW/cm^2) more than when using idealistic sinusoidal voltages, while the corresponding efficiency increased from 13.4 % to 28.9 %. Fig. 9b clearly shows that the fraction of power deposition through the electrons using distorted bipolar square voltages is nearly 2 times greater (22.7 % to 43.5 %) than when using idealistic sinusoidal voltages. In other words, the fraction of total power deposition through the two types of ions decreased from 76.9 % (sinusoidal case) to 56.5 % (distorted bipolar square case). Note that this dramatic increase of power deposition through the electrons is responsible for the large increase of the 172 nm VUV emission, as found in Fig. 9a, in which the energetic electrons efficiently excited the ground-state xenon and generated much more abundant excimers to emit 172 nm VUV photons.

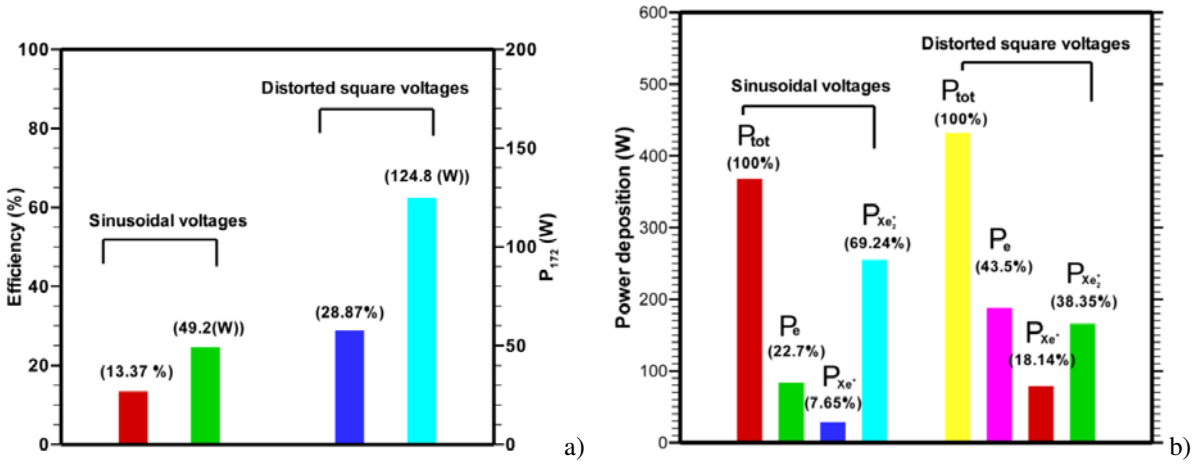

Fig. 9 The efficiency and P172 under different power source. (b) The deposition power and power partition under different power source.

To further understand the reason for the increase in VUV emission using distorted bipolar square voltages as compared to idealistic sinusoidal voltages, phase diagrams of 172 nm VUV emission power distribution for both cases are shown in Fig. 10. The results show that VUV emission occurred much earlier, with greater intensity and more uniformity across the whole gap during the discharge process in the former case. This is attributed to the rapidly rising voltage of the distorted bipolar square voltages and thus, higher energy absorption efficiency by the electrons, which then generated abundant Xe*(met) and, thus $Xe_2^*(^3\sum_u^+)$ for the 172 nm VUV photon emission.

Fig. 11 shows the temporal variation of power deposition through the charged species along with the gap voltage of the sinusoidal case. It is found, for example, that in the first half cycle (Period II-1), the electron power deposition of distorted bipolar square voltages is much higher than that of the sinusoidal ones (see bottom of Fig. 8) (45 Wcm^{-3} vs. 13 Wcm^{-3}) because of the much larger $|dV_g/dt|$ ($\sim$ 3.8 times) in the pre-discharge period. The larger value of $|dV_g/dt|$ represents the shorter period prior to the breakdown gap voltage ($\sim$ 2.4 kV), during

which only the electrons could respond instantly (almost without inertia) and gain energy from the field efficiently without much elastic collision loss. This is shown in Fig. 12, in which the electrons gain energy through ohmic heating and lose energy mostly through inelastic collisions, especially the excitations of ground-state xenon (No. 4 and 5 in Table 1). In the case of distorted bipolar square voltages, the electron temperature in Period I increased up to $\sim$ 4 eV (see Fig. 7), while it only reached 2-3 eV in the case of sinusoidal voltages (not shown here). This also explained why the atomic xenon ions absorbed the energy with some phase lag, as compared to the electrons, because of the inertia effects in both cases. As for the power deposition through Xe_2^+, it is still quite appreciable and extended for a relatively long period, even in the post-discharge period for the sinusoidal case; this is caused by non-vanishing gap voltages in this period which are beneficial for the power absorption of Xe_2^+, unlike the nearly vanishing gap voltage in the same period for the case of distorted bipolar square voltages. In addition, Figure 12 shows that the divergence of electron energy flux density deviates from zero, this quantity indicates a real transport effect in the range of r = 0.95 to 1.02 and values in the range r = 0.8 to 0.9 may be affected by numerical inaccuracy caused by known difficulties in evaluation of divergence terms which demonstrates that use of non-local electron energy density equation for a proper fluid modeling of xenon discharge is necessary in the present study.

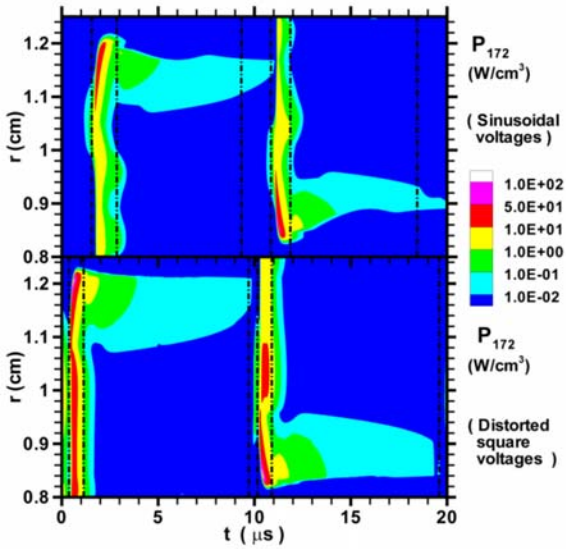

Fig. 10 The comparison of light power emission (P_{172}) between sinusoidal voltages (the upper figure) and distorted square voltages (the bottom figure).

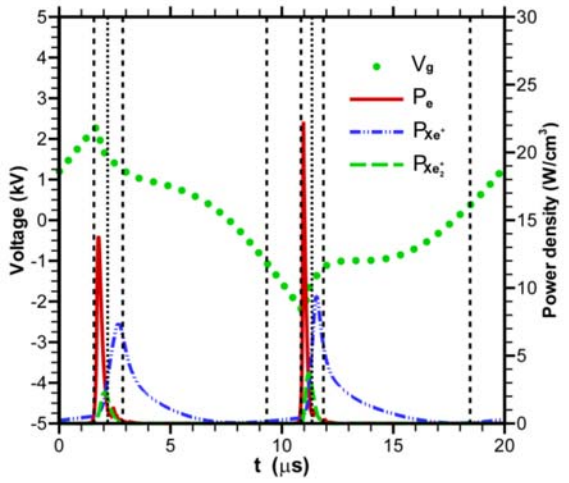

Fig. 11 The variation of power deposition of charged species in a xenon excmier discharge using sinusoidal voltages.

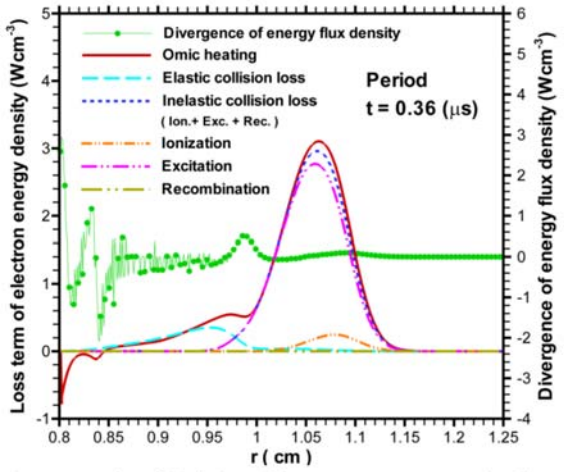

Fig. 12 A snapshot of distributions of electron energy components using distorted square voltages.

4 Conclusion

In this paper, enhancement of vacuum UV emission from a coaxial xenon excimer UV lamp (EUV) driven by 50 kHz distorted bipolar square voltages, rather than by sinusoidal voltage waveforms, has been investigated numerically. A self-consistent radial one-dimensional fluid model, taking into consideration non-local electron energy balance, is employed to simulate the complicated discharge physics and chemistry. The discharge is divided into two portions of three breakdown periods, which included the pre-discharge, the discharge (most intense 172 nm VUV emission) and the post-discharge periods. An interesting "cathode-directed streamer-like" ionization wave, having atomic xenon ions at the head and the electrons at the tail, is found to move at a speed of $\sim$ 7,000 m/s in the early part of the discharge period (Period II-1).

The results show that the efficiency of VUV emission using distorted bipolar square voltages is much higher than that using sinusoidal voltages (28.9 % vs. 13.4 %). This is attributed to the two following two mechanisms. The first is the greater rate of voltage increase in bipolar square voltages as compared to sinusoidal voltages, which allowed only electrons to efficiently absorb the power in a short period of time without much elastic collision loss. Energetic electrons then generated higher amounts of excimer (and also metastable) xenon with more uniform distribution across the gap for a longer period of time during the discharge process. The second is the comparably smaller amount of "wasted" power deposition by Xe_2^+ in the post-discharge period driven by distorted bipolar square voltages because of the nearly vanishing gap voltage, which is caused by the shielding effect due to the accumulated charges on both dielectric surfaces.

Acknowledgements The authors are grateful for the financial support of the National Science Council of Taiwan (NSC 96-2628-E-009-134-MY3), ITRI/MCL, through Dr. Bee-Yu Wei, Institute of Nuclear Energy Research (992001INER028), and the Ministry of Economic Affairs of Taiwan.

References

[1] B. Eliasson, U. Kogelschatz, Appl. Phys. B **46**, 299 (1988).
[2] D.M. Kane, D. Hirschausen, B.K. Ward, R.J. Carman, R.P. Mildren, Proc. of SPIE **5399**, 100 (2004).
[3] J.H. Park, I.K. Lee, B.H. Cho, J.K. Lee, K.W. Whang, PCC07 (Nagoya), 717 (2007).
[4] T. Shiga, S. Mikoshiba, S. Shinada, Elec. and Comm. in Japan **84**, 55 (2001).
[5] E. Safta, US Patent 6767458, 2004.
[6] C.K. Buck, A.J. Pedraza, R.S. Benson, J.W. Park, Nucl. Instrum. Methods Phys. Res. B **141**, 675 (1998).
[7] J.Y. Zhang, I.W. Boyd, J. Appl. Phys. **80**, 633 (1996).
[8] S. Stockwald, M. Neiger, Contrib. Plasma Phys. **35**, 15 (1995).
[9] F. Vollkommer, L. Hitzschke, US Patent 5604410 1997.
[10] A. Oda, Y. Sakai, H. Akashi, H. Sugawara, J. Phys. D: Appl. Phys. **32**, 2726 (1999).
[11] G.N. Zvereva, G.N. Gerasimov, Optics and Spectroscopy **90**, 321 (2001).
[12] R.J. Carman, R.J. Mildren, Phys. D: Appl. Phys. **36**, 19 (2003).
[13] S. Beleznai, G. Mihajlik, A. Agod, I. Maros, R. Juhasz, Z. Nemeth, L. Jakab, P. Richer, J. Phys. D: Appl. Phys. **39**, 3777 (2006) .
[14] S.V. Avtaeva, E.B. Kulumbaev, Plasma physics reports **34**, 452 (2008).
[15] S.Y. Jou, C.T. Hung, Y.M. Chiu, J.S. Wu, B.Y. Wei, Plasma Chem Plasma Process **30**, 907 (2010).
[16] C.-T. Hung, Y.-M. Chiu, F.-N. Hwang, J.-S. Wu, Computer Physics Communications **182**, 161 (2011).
[17] Y.P. Raizer, Gas discharges Physics (Springer Verlag, Berlin, 1991).

